# Nuclear Physics Meets the Sources of the Ultra-High Energy Cosmic Rays

Denise Boncioli, Anatoli Fedynitch, and Walter Winter
*DESY, Platanenallee 6, D-15738 Zeuthen, Germany*
(Dated: August 5, 2016)

We study the implications of nuclear data and models for cosmic-ray astrophysics, which involves the photodisintegration of nuclei up to iron in astrophysical environments. We demonstrate that data on photo-absorption cross sections are sparse in that mass range by screening nuclear databases, such as EXFOR; these cross sections are needed to compute the photodisintegration rates. We also test the prediction power of models, such as TALYS, and find uncertainties of the order of a factor two. If however the radiation fields are strong enough such that the nuclear cascade in the astrophysical source can develop, we find that differences among different models average out – unless there is a systematic offset in the interaction model. We conclude with an isotope chart describing which information is in principle necessary to describe nuclear interactions, supported by simulating the entire disintegration chain in a gamma-ray burst. We also point out that a first consistency check may be the measurement of the absorption cross section for different isobars.



**Introduction.** Particles from space reaching the Earth with energies higher than $10^9$ GeV are detected by ultra-high energy cosmic-ray (UHECR) observatories such as the Pierre Auger Observatory [1] and the Telescope Array (TA) experiment [2]. UHECRs are expected to be accelerated in astrophysical sources and to travel through extragalactic space before they hit the Earth's atmosphere; they can interact with photons in both environments. The primary composition of UHECRs is still unknown; however, the mass composition measured by the Auger Observatory indicates heavier elements at the highest energies beyond $10^{9.3}$ GeV [3], *i.e.*, significantly heavier than helium and at most as heavy as iron. The study of interactions of nuclei is therefore critical for our understanding of cosmic-ray astrophysics both within sources and during propagation.

In this letter, we focus on the photodisintegration of nuclei, which has been extensively studied in extragalactic photon fields as the cosmic microwave background (CMB) and the extragalactic background light (EBL), where it is the dominant process changing the mass composition of the nuclei. The leading contribution to photodisintegration is an excitation called "giant dipole resonance" (GDR) [4], which can be interpreted as a vibration of the bulk of protons and neutrons leading to a resonant structure. This process occurs above ∼8 MeV (energy in the nucleus' rest frame) and causes the disruption of the primary nucleus with the emission of one or two nucleons. At higher energies the "quasi-deuteron" (QD) process dominates, where the photon interacts with a nucleon pair followed by consequent ejection of two or more nucleons.

A frequently used model in cosmic-ray astrophysics is Puget-Stecker-Bredekamp (PSB) [5], that relies on choosing one isotope for each mass number $A$, and a unique disintegration chain populated through subsequent emission of nucleons. This approach is implemented for cosmic-ray propagation in the *SimProp* software [6]. A more sophisticated approach, based on the TALYS nuclear reaction program [7], is implemented in the cosmic-ray propagation software CRPropa3 [8], which includes 183 isotopes and 2200 channels for the photodisintegration. Differences in modeling the interactions affect the observables (as energy spectrum and composition), and consequently have an impact on the interpretation of UHECR measurements [9, 10].

UHECRs are expected to be accelerated in astrophysical sources, such as Gamma-Ray Bursts (GRBs), and will interact with their photon field; see Ref. [11] for a review. Examples for disintegration treatments include [12, 13], where the GDR modeling follows [14] with a modified Gaussian parametrization of cross sections from [5]. The GDR resonance is even more simplified in [15–17] as a box function. Other authors use semi-analytical implementations of existing UHECR propagation codes (such as CRPropa) [18]. It is probably fair to say that the interactions in the sources have not been modeled with a complexity comparable to cosmic-ray propagation. That can be attributed to the fact that the target photon spectrum, relevant for the photodisintegration, is *a priori* arbitrary, *i.e.*, it can have a very different shape compared to that of the CMB.

In this work, we present a description of the sources with a level of complexity of the interactions comparable to that of the most sophisticated cosmic-ray propagation models. We review the available nuclear data necessary to construct and verify reliable interaction models, and we point out what information is missing from nuclear physics.

**Situation on Experimental Data and Theoretical Models.** The experimental situation on photonuclear cross section data is shown in Fig. 1, based on data from the most complete EXFOR database [20]; for details see App. B. Of particular interest are measurements of the following cross sections in the GDR and QD energy bands ($E_\gamma < 150$ MeV): the total photoabsorption cross sections $\sigma_{\rm abs}$ (red boxes), the residual nucleus cross sections, such as $\sigma_{^{27}{\rm Al}}(\gamma, X + {}^{24}{\rm Na})$ (where $X$ refers to any combination secondaries), and the inclusive light fragment cross sections, such as the neutron yield $\sigma_{^{27}{\rm Al}}(\gamma, x \cdot {\rm n})$). In the following we refer to residual and light fragment cross sections as *inclusive* cross sec-

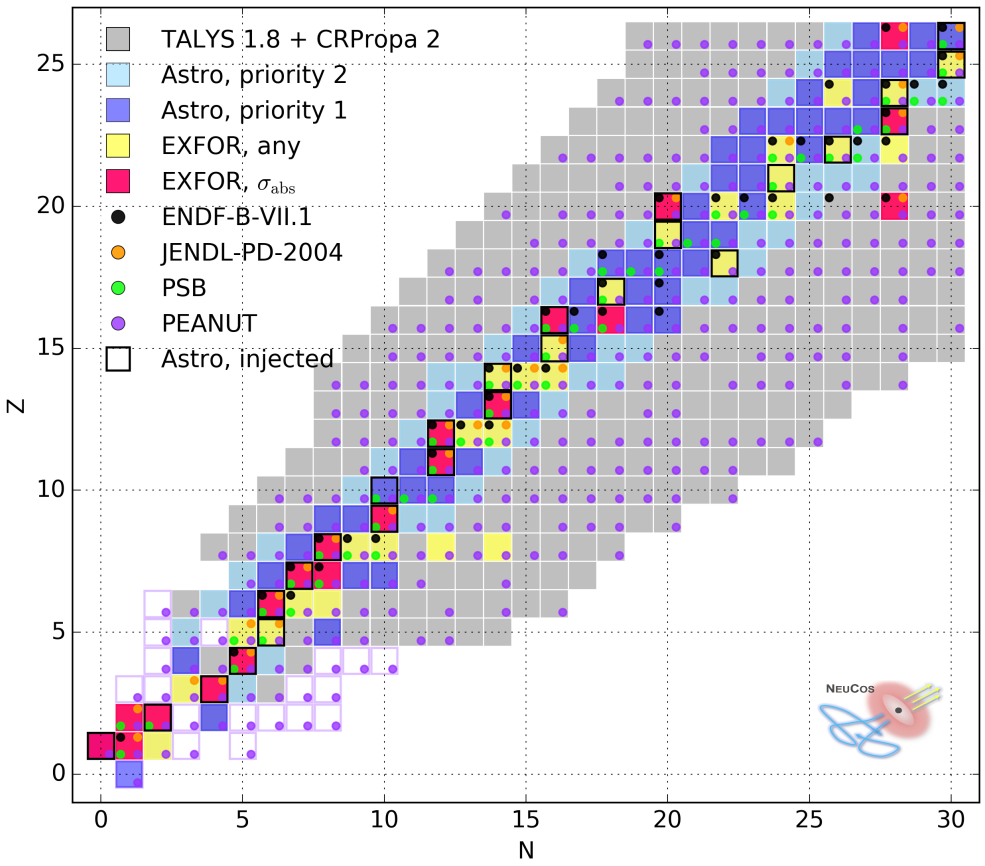


FIG. 1: Experimental situation versus astrophysical requirements for nuclear isotopes interesting for cosmic-ray astrophysics (gray boxes, from TALYS [7] and CRPropa2 [19]). Experimental measurements (from EXFOR database [20]) are marked by red (yellow) boxes if the total absorption (any inclusive cross section) has been measured. Theoretical models are marked by dots (ENDF [21], JENDL [22], PEANUT [23, 24], PSB [5]). Calculations in cosmic-ray astrophysics require the total and inclusive cross sections for the blue isotopes. Injected isotopes are framed by black rectangles (most abundant stable isotopes chosen). White boxes refer to very unstable isotopes integrated out in the disintegration chain.

tion $\sigma^{\rm incl}_{^{27}{\rm Al}\to^{24}{\rm Na}}$ or $\sigma^{\rm incl}_{^{27}{\rm Al}\to n}$, respectively (yellow boxes, if at least one of these measured). Data are sparse, and mostly available for stable elements along the main diagonal. An outstanding feature is that we did not find any $\sigma_{\rm abs}$ measurement for isobars, *i.e.*, two elements with the same mass number $A$. Note that in astrophysical environments, unstable isotopes gain importance, since all kinds of secondary nuclei are created in the disintegration chain and their lifetime is dilated by the relativistic boost. Therefore, these radioactive nuclei can re-interact with the photon field and create secondaries within the lifetime of the system.

We also show the availability of nuclear models and data files in Fig. 1, that use interpolated or fitted $\sigma_{\rm abs}$ where measurements are available, see App. B. Unmeasured $\sigma_{\rm abs}$ are obtained from model evaluations of photo-neutron cross sections where available, otherwise from empirical parameterizations [23], implying that, in the absence of data, the cross sections further off the main diagonal are uncertain. Inclusive reaction cross sections are calculated with numerical or Monte Carlo internuclear cascade-preequilibrium-evaporation (ICPE) codes, and are partially fine-tuned to data on branchings.

**Cross sections and photo-nuclear disintegration rates.** We illustrate the situation on cross sections in Fig. 2, upper panels, where we pick two isobar nuclei with $A = 40$: $^{40}$Ca is a double magic nuclide for which one photo-absorption cross section measurement is available [25], while $^{40}$Ar is expected to have different properties due to a different shell structure. Fig. 2 demonstrates that the TALYS predictions are almost independent of the isotope, while PEANUT, the FLUKA code [26, 27] relies on, shows substantial changes between $^{40}$Ca to $^{40}$Ar and reproduces the data for $^{40}$Ca. The low-energy and high energy peaks observed in data are virtually not present in the models. The PSB cross section is, by definition, the same for isobar nuclei. The expected uncertainty among different models is of order two, where

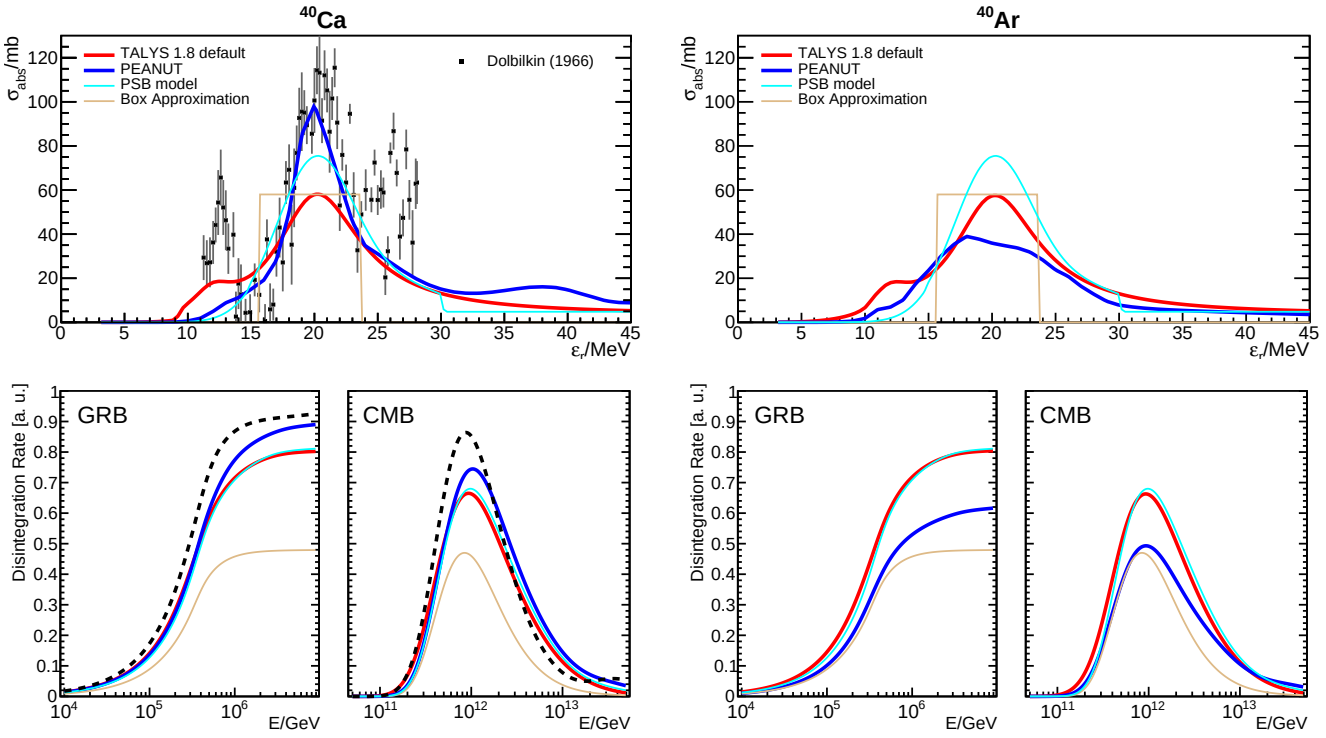


FIG. 2: Comparison of cross sections (upper row) and disintegration lengths (lower row) for two different isobars (columns) with $A = 40$. The total absorption cross sections for photodisintegration are shown as a function of the energy $\varepsilon_r$ in the nucleus' rest frame, where data are shown if available. The different curves correspond to models as given in the plot legend, where the GDR box approximation is based in the assumptions in Ref. [15]. The corresponding disintegration rates are calculated for two different target photon spectra: for the GRB spectrum, a broken power law with spectral indices $-1$ and $-2$ and a break at 1 keV (energies in shock rest frame) has been assumed, whereas the CMB spectrum refers to the cosmic microwave background at redshift zero, *i.e.*, a thermal target photon spectrum with $T = 2.73$ K. Dashed lines refer to disintegration rates calculated for measured cross sections.

smilar results are found in other cases (an alternative case $A = 23$ is described in App. D).

Here we illustrate the consequences of the experimental data availability and the prediction power of the models at the example of the photodisintegration rate $\Gamma \sim c\, n_\gamma\, \sigma$ (see App. A for details of the computation). The disintegration rates $\Gamma$ are indicative for the optical thickness for cosmic-ray escape from the source $\tau = R \cdot \Gamma / c$ (where $R$ is the source size). They are shown for two astrophysical environments, CMB and GRB, in the lower panels of Fig. 2 – corresponding to the cross sections in the upper panels. The uncertainties in the cross sections translate into similar uncertainties of the disintegration rates, which are sensitive to both the width and the threshold of the cross section peak(s). However, the effect from multiple peaks smears out due to pitch angle averaging related to the (assumed) isotropic target photon distribution. Note that the relative impact of the models is qualitatively similar for the different target photon fields, but the quantitative impact can be larger for environments different from the CMB, which are more sensitive to the high-energy part of the cross section – see GRB example.

Astrophysical applications require predictability of the cross sections, while the models are not always designed for that; as a consequence, we find apparent differences for individual isotopes. For example, total absorption cross sections seem consistently alike for different isobars in TALYS (unless tuned to a measurement), whereas differences are in some cases expected and predicted in PEANUT – such as between $^{40}$Ca, which is double-magic, and $^{40}$Ar.

**Effect on the nuclear cascade.** Let us now discuss the extreme case of strong disintegration: We show in Fig. 3 the effect of photodisintegration of $^{56}$Fe in a GRB for the PSB and TALYS models, where the parameters have been chosen such that the target photon density is high enough to observe the cascade. Details of the GRB model and alternative model assumptions are presented in App. C.

For the PSB model, there is only one isotope for each $A$; as a consequence the required nuclear physics input is "one dimensional" ($\sigma_{\rm abs}$ plus limited branching information). Neutrons and protons are strongly populated, since they are created in each interaction. The TALYS

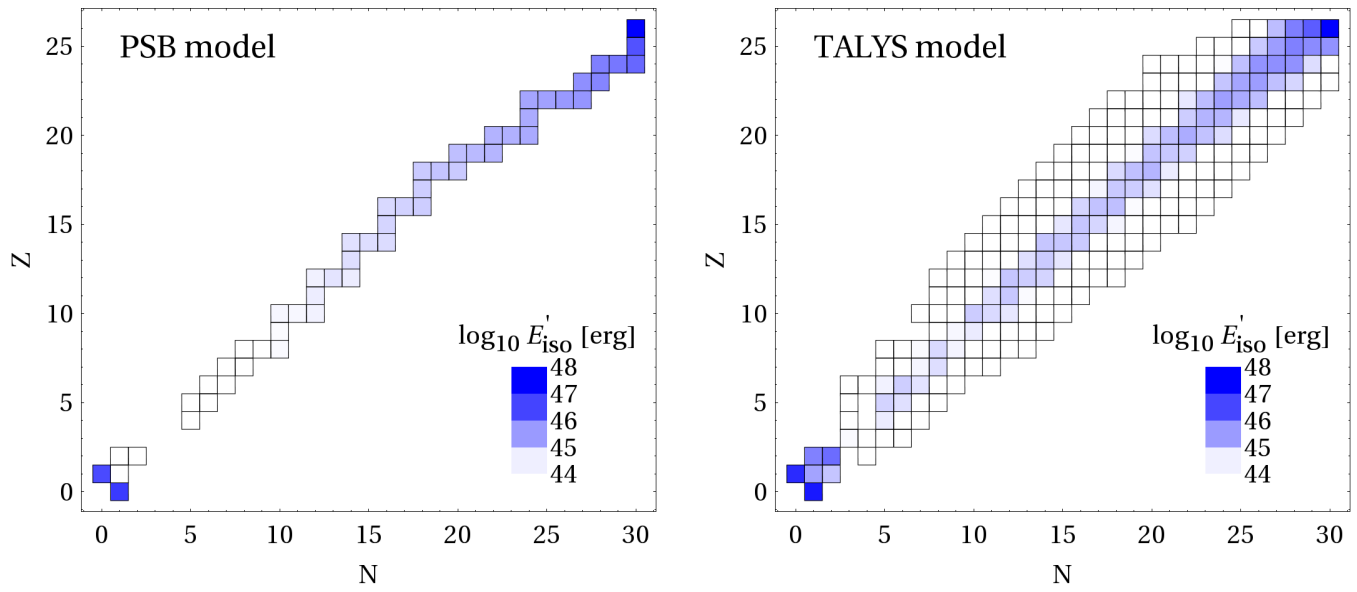


FIG. 3: Disintegration of $^{56}$Fe in a shell of a GRB, where the population of isotopes (in terms of the total energy per isotope and collision in the shock rest frame) is shown. The different panels correspond to the PSB [5] and TALYS [7] (and CRPropa [19] for the lighter elements) models. The GRB parameters are $L_{\gamma,\rm iso} = 10^{52}\,\rm erg/s$, $\Gamma = 300$, $t_v = 0.01\,\rm s$, $z = 2$, and $E_{\rm Fe,max} \simeq 10^{11}\,\rm GeV$ (in the observer's frame).

model predicts the population of isotopes off the main diagonal, and in addition, significantly more light (such ad $^4$He) and intermediate ($10 \lesssim A \lesssim 20$) nuclei, which are produced in high-energy processes.

It is interesting to discuss the consequences for physical observables; we show the emitted cosmic-ray composition from the GRB in Fig. 4. First of all, it is noteworthy that the observed UHECR composition [3] can be roughly reproduced from a single GRB shell and iron injection only, and will be even smoother after propagation. More sophisticated interaction models (TALYS, PEANUT) produce similar results, and even random cross section offsets within the model uncertainties do not qualitatively affect this picture, as the random variations seem to average out over the large number of involved isotopes (see shaded region for 100 ensemble models). However, the lack of/feeddown into light and intermediate elements produced in the PSB and "systematic offset" (systematic suppression of all unmeasured cross sections) models leads to strong deviations at about $10^{10}\,\rm GeV$ from the baseline models. From this example, we conclude that the interaction model needs to be more sophisticated than the PSB model with a prediction power good enough to avoid systematic offsets. Note that such systematic offsets can also occur if a subset of isotope cross sections in the model is adjusted to measurements, while leaving the bulk of other unmeasured isotopes unmodified. Since neutrons can easier escape from the astrophysical source than protons, the cosmic ray composition is sensitive to an artificial imbalance between proton- and neutron-rich elements in the cascade.

We derive a complete list of isotopes for which the absorption and inclusive cross sections are needed to cover any cosmic-ray astrophysics scenario involving injection elements with masses up to iron, that we separate in "Astro, priority 1" and "Astro, priority 2" in Fig. 1 (see App. C for details); it is apparently consistent with the isotopes populated in Fig. 3. This information could come from predictive models, or from measurements directly. The certainty in predictive power for cross sections may be improved by systematic measurements using isotope groups along the main diagonal and perpendicular to it (isobars), such as $^{40}$Ar in addition to $^{40}$Ca (other stable isobar pairs are $^{36}$S/$^{36}$Ar, $^{46}$Ca/$^{46}$Ti, $^{50}$Ti/$^{50}$Cr, and $^{54}$Cr/$^{54}$Fe).

**Summary and conclusions.** We have compared the situation of nuclear measurements (red/yellow in Fig. 1) with the input needed for cosmic-ray astrophysics (blue in Fig. 1), where we have included astrophysical sources as a key aspect in addition to conventional studies on cosmic-ray propagation. We have demonstrated that the measurements on the participating nuclear isotopes are sparse, as unstable nuclei are produced in the photodisintegration which can live relatively long at extremely high energies where their lifetimes are Lorentz-boosted.

While sophisticated nuclear models exist, such as TALYS, their prediction power for low mass (lower than iron) isotopes seems limited to within about a factor of two. While the impact on individual photodisintegration rates can be large, we have found that random fluctuations do not affect the nuclear cascade unless there are systematic effects not probably accounted for, such as offsets between neutron- and proton-rich elements, along the main diagonal, or a missed feeddown into lighter iso-

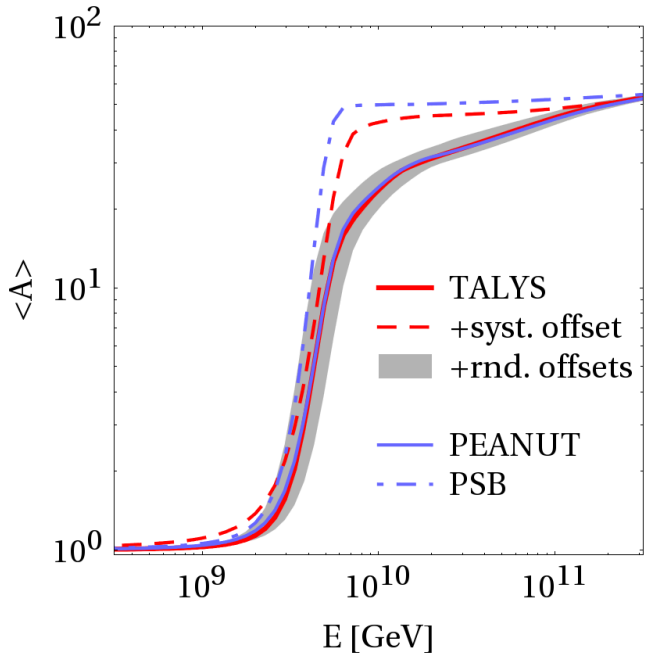


FIG. 4: Emitted cosmic-ray composition from a GRB as a function of observed energy without propagation effects for various nuclear disintegration models (same parameters as in Fig. 3, iron injection only). Here it is assumed that cosmic-ray nuclei either escape as neutrons from the source (which leads to escape spectra $\propto E^{-2}$), or as charged particles if they can reach the outside of the source within their Larmor radius ("direct escape", which leads to harder escape spectra $\propto E^{-1}$, see Ref. [28]). The shaded region shows the model spread for an ensemble of 100 variations of the TALYS model with random cross section offsets (per isotope) within the anticipated uncertainty, and the "systematics offset" curve refers to a systematic suppression of all unmeasured cross sections, see App. C for details.

topes. We therefore propose systematic measurements to improve the predictability of unmeasured cross sections, such as by measuring the total absorption cross section for two or more different isobars – for which we did not find a single existing example. A long term goal could be measurements of total and inclusive cross sections of the blue-marked isotopes in Fig. 1.

**Acknowledgments.** We would like to thank Alfredo Ferrari for enlightening discussions and the permission to use PEANUT for our purpose. We thank also B. Kämpfer, A.R. Junghans and R. Schwengner from Helmholtz-Zentrum Dresden-Rossendorf for interesting discussions.

This project has received funding from the European Research Council (ERC) under the European Union's Horizon 2020 research and innovation programme (Grant No. 646623).

[1] A. Aab and et al. [Pierre Auger Collaboration], Nucl. Instrum. Meth. **A798**, 172 (2015), arXiv:1502.01323 [astro-ph.IM] .
[2] T. Abu-Zayyad et al. [Telescope Array Collaboration], Nucl. Instrum. Meth. **A689**, 87 (2013), arXiv:1201.4964 [astro-ph.IM].
[3] A. Porcelli et al. [Pierre Auger Collaboration] (PoS(ICRC2015)420, 2015).
[4] M. Goldhaber and E. Teller, Phys. Rev. **74**, 1046 (1948).
[5] J. L. Puget, F. W. Stecker, and J. H. Bredekamp, Astrophys. J. **205**, 638 (1976).
[6] R. Aloisio, D. Boncioli, A. di Matteo, A. Grillo, S. Petrera, and F. Salamida, (2016), arXiv:1602.01239 [astro-ph.HE] .
[7] A. J. Koning, S. Hilaire, and M. C. Duijvestijn, in *Proceedings, International Conference on Nuclear Data for Science and Tecnology* (2007) pp. 211–214.
[8] R. A. Batista, A. Dundovic, M. Erdmann, K.-H. Kampert, D. Kuempel, G. Müller, G. Sigl, A. van Vliet, D. Walz, and T. Winchen, JCAP **1605**, 038 (2016), arXiv:1603.07142 [astro-ph.IM] .
[9] R. Alves Batista, D. Boncioli, A. di Matteo, A. van Vliet, and D. Walz, JCAP **1510**, 063 (2015), arXiv:1508.01824 [astro-ph.HE] .
[10] A. di Matteo et al. [Pierre Auger Collaboration] (PoS(ICRC2015)249, 2015).
[11] P. Meszaros, Rept. Prog. Phys. **69**, 2259 (2006), arXiv:astro-ph/0605208 [astro-ph].
[12] N. Globus, D. Allard, R. Mochkovitch, and E. Parizot, Mon. Not. Roy. Astron. Soc. **451**, 751 (2015), arXiv:1409.1271 [astro-ph.HE] .
[13] L. A. Anchordoqui, D. Hooper, S. Sarkar, and A. M. Taylor, Astropart. Phys. **29**, 1 (2008), arXiv:astro-ph/0703001 [astro-ph] .
[14] E. Khan, S. Goriely, D. Allard, E. Parizot, T. Suomijarvi, A. J. Koning, S. Hilaire, and M. C. Duijvestijn, Astropart. Phys. **23**, 191 (2005), arXiv:astro-ph/0412109 [astro-ph] .

[15] K. Murase and J. F. Beacom, Phys. Rev. **D81**, 123001 (2010), arXiv:1003.4959 [astro-ph.HE] .

[16] K. Murase, K. Ioka, S. Nagataki, and T. Nakamura, Phys.Rev. **D78**, 023005 (2008), arXiv:0801.2861 [astro-ph] .

[17] M. Bustamante, P. Baerwald, K. Murase, and W. Winter, Nature Commun. **6**, 6783 (2015), arXiv:1409.2874 [astro-ph.HE] .

[18] M. Unger, G. R. Farrar, and L. A. Anchordoqui, Phys. Rev. **D91**, 092008 (2015) arXiv:1505.02153 [astro-ph.HE] .

[19] K.-H. Kampert, J. Kulbartz, L. Maccione, N. Nierstenhoefer, P. Schiffer, G. Sigl, and A. R. van Vliet, Astropart. Phys. **42**, 41 (2013), arXiv:1206.3132 [astro-ph.IM] .

[20] N. Otuka, E. Dupont, V. Semkova, B. Pritychenko, A. Blokhin, M. Aikawa, S. Babykina, M. Bossant, G. Chen, S. Dunaeva, R. Forrest, T. Fukahori, N. Furutachi, S. Ganesan, Z. Ge, O. Gritzay, M. Herman, S. Hlavač, K. Kato, B. Lalremruata, Y. Lee, A. Makinaga, K. Matsumoto, M. Mikhaylyukova, G. Pikulina, V. Pronyaev, A. Saxena, O. Schwerer, S. Simakov, N. Soppera, R. Suzuki, S. Takács, X. Tao, S. Taova, F. Tárkányi, V. Varlamov, J. Wang, S. Yang, V. Zerkin, and Y. Zhuang, Nuclear Data Sheets **120**, 272 (2014).

[21] M. Chadwick, M. Herman, P. Obložinský, M. Dunn, Y. Danon, A. Kahler, D. Smith, B. Pritychenko, G. Arbanas, R. Arcilla, R. Brewer, D. Brown, R. Capote, A. Carlson, Y. Cho, H. Derrien, K. Guber, G. Hale, S. Hoblit, S. Holloway, T. Johnson, T. Kawano, B. Kiedrowski, H. Kim, S. Kunieda, N. Larson, L. Leal, J. Lestone, R. Little, E. McCutchan, R. MacFarlane, M. MacInnes, C. Mattoon, R. McKnight, S. Mughabghab, G. Nobre, G. Palmiotti, A. Palumbo, M. Pigni, V. Pronyaev, R. Sayer, A. Sonzogni, N. Summers, P. Talou, I. Thompson, A. Trkov, R. Vogt, S. van der Marck, A. Wallner, M. White, D. Wiarda, and P. Young, Nuclear Data Sheets **112**, 2887 (2011), special Issue on ENDF/B-VII.1 Library.

[22] N. Kishida, T. Murata, T. Asami, K. Kosako, K. Maki, H. Harada, Y. Lee, J. Chang, S. Chiba, and T. Fukahori, AIP Conference Proceedings **769**, 199 (2005).

[23] A. Fassò, A. Ferrari, and P. R. Sala, Proc. SATIF-3, Sendai, Japan , 61 (1997).

[24] A. Fassò, A. Ferrari, and P. R. Sala, AIP Conference Proceedings **769**, 1303 (2005).

[25] B. S. Dolbilkin, V. A. Zapevalov, V. I. Korin, L. E. Lazareva, and F. A. Nikolaev, Bull. Russian Academy of Sciences - Physics **30** (1966).

[26] A. Ferrari, P. R. Sala, A. Fasso, and J. Ranft, CERN-2005-010 (2005).

[27] T. Böhlen, F. Cerutti, M. Chin, A. Fassò, A. Ferrari, P. Ortega, A. Mairani, P. Sala, G. Smirnov, and V. Vlachoudis, Nuclear Data Sheets **120**, 211 (2014).

[28] P. Baerwald, M. Bustamante, and W. Winter, Astrophys. J. **768**, 186 (2013), arXiv:1301.6163 [astro-ph.HE] .

[29] J. T. Goorley, M. R. James, T. E. Booth, F. B. Brown, J. S. Bull, L. J. Cox, J. W. J. Durkee, J. S. Elson, M. L. Fensin, R. A. I. Forster, *et al.*, *Initial MCNP6 Release Overview - MCNP6 version 1.0*, Tech. Rep. LA-UR-13-22934 (2013).

[30] T. Sato, K. Niita, N. Matsuda, S. Hashimoto, Y. Iwamoto, S. Noda, T. Ogawa, H. Iwase, H. Nakashima, T. Fukahori, K. Okumura, T. Kai, S. Chiba, T. Furuta, and L. Sihver, Journal of Nuclear Science and Technology **50**, 913 (2013),.

[31] F. W. Stecker and M. H. Salamon, Astrophys. J. **512**, 521 (1999), arXiv:astro-ph/9808110 [astro-ph] .

[32] S. Hümmer, P. Baerwald, and W. Winter, Phys. Rev. Lett. **108**, 231101 (2012), arXiv:1112.1076 [astro-ph.HE] .

[33] D. Boncioli, A. Fedynitch, and W. Winter, In preparation.

[34] A. Mucke, R. Engel, J. Rachen, R. Protheroe, and T. Stanev, Comput. Phys. Commun. **124**, 290 (2000), arXiv:astro-ph/9903478 [astro-ph] .

[35] S. Hümmer, M. Rüger, F. Spanier, and W. Winter, Astrophys. J. **721**, 630 (2010), arXiv:1002.1310 [astro-ph.HE] .

[36] Wolfram, "Mathematica software, IsotopeData," (2016), see `http://reference.wolfram.com/language/note/IsotopeDataSourceInformation.html`.

[37] D. Biehl, D. Boncioli, A. Fedynitch, and W. Winter, In preparation.

[38] B. S. Ishkhanov, I. M. Kapitonov, V. I. Shvedunov, A. I. Gutiy, and A. M. Parlag, Yadernaya Fizika **33**, 581 (1981).

## SUPPLEMENTAL MATERIAL

### Appendix A: Cross section terminology and computation of disintegration lengths

Numerical solutions of our system of Boltzmann transport equations (see App. C) require knowledge about the rate of interactions and the average outcome of the bulk of all possible reactions. The interaction rate $\Gamma_j$ of the primary nucleus $j$ is used to compute the secondary injection and primary escape flux. The interaction rate depends on the interaction partner, the photon, as

$$\Gamma_j(E_j) = \int d\varepsilon \int_{-1}^{+1} \frac{d\cos\theta_{j\gamma}}{2} (1-\cos\theta_{j\gamma}) \cdot \cdot n_\gamma(\varepsilon, \cos\theta_{j\gamma})\, \sigma_j^{\rm abs}(\epsilon_r)\,. \quad \text{(A1)}$$

Here $n_\gamma(\varepsilon, \cos\theta_{j\gamma})$ is the photon density as a function of photon energy $\varepsilon$ and the (pitch) angle between the photon and proton momenta $\theta_{j\gamma}$, $\sigma_j^{\rm abs}(\epsilon_r)$ is the absorption cross section and

$$\epsilon_r = \frac{E_j\,\varepsilon}{m_j}(1-\cos\theta_{j\gamma}) \quad \text{(A2)}$$

is the photon energy in the parent rest frame (PRF) or nucleus rest frame in the limit $\beta_A \approx 1$, and can be directly related to the available center-of-mass energy. The interaction itself, and therefore $E_j$ and $\varepsilon$, is typically defined in the shock rest frame (SRF). Eq. (A2) clearly shows that the relevant energy range in the PRF is defined by the product of the target photon's energy times the nucleus energy in the SRF and is therefore highly dependent on both, the choice of the target photon and the injection spectrum. In our models we assume isotropy $n_\gamma(\varepsilon, \cos\theta_{p\gamma}) \simeq n_\gamma(\varepsilon)$ of the target photon distribution. This means that, for GRBs, we compute the interactions in the shock rest frame where isotropy occurs if the target photons come from self-consistent internal radiation processes (such as synchrotron emission of electrons/positrons). Isotropy smears out the substructure of the energy dependence of $\sigma_{\rm abs}$.

The injection $j \to i$ of secondaries $Q_{ji}$, which we need in Eq. (C2), is given by

$$Q_{ji}(E_i) = \int dE_j\, N_j(E_j)\, \frac{d\Gamma_{ji}(E_j)}{dE_i}\,, \quad \text{(A3)}$$

where $d\Gamma_{ji}(E_j)/dE_i$ can be obtained from Eq. (A1) by replacing the total absorption cross section with the differential inclusive cross section

$$\sigma_j^{\rm abs}(\epsilon_r) \to \frac{d\sigma_{j\to i}^{\rm incl}}{dE_i} \equiv \sigma_j^{\rm abs}(\epsilon_r)\, \frac{dn_{j\to i}}{dE_i}\,, \quad \text{(A4)}$$

where $dn_{j\to i}/dE_i$ is the re-distribution function of the secondaries. For the energy spectrum of secondaries, we make use of typical kinematics, where for example, for GRBs, the nuclei have PeV energies and the photons are in keV range. In that case the momentum transfer on the ejected secondaries is small compared to $E_j$, resulting in an approximate conservation of the relativistic boost. In that case, the re-distribution function can be approximated as a function of $\epsilon_r$ and $E_i/E_j$ as

$$\frac{dn_{j\to i}}{dE_i} \simeq M_{j\to i}(\epsilon_r) \cdot \delta\left(E_i - \frac{m_i}{m_j}E_j\right)\,, \quad \text{(A5)}$$

where $M_{j\to i}$ is the average number of secondaries produced per interaction (also called "multiplicity"). It can be related to the exclusive reaction cross sections, summed over all channels in which the species $i$ is produced, as

$$M_{j\to i} = \frac{1}{\sigma_j^{\rm abs}} \sum_{X_n} N_i\, \sigma_j^{\rm excl}(\gamma, X_n + i)\,, \quad \text{(A6)}$$

where $N_i$ is the number of secondaries $i$ in that exclusive channel. Note that the ratio between exclusive and total absorption cross section corresponds to the branching ratio. While for light fragments, $M$ can be larger than one, one expects for residual nuclei $M \lesssim 1$.

Finally, note that fixed target experiments in photon beams typically measure the cross section in terms of PRF energy, and it is a frequently asked question up to which energy the cross section needs to be measured. In astrophysical environments, a certain PRF energy can be related to the primary $E_j$ and photon $\varepsilon$ energies by the estimate $\epsilon_r \sim E_j\,\varepsilon/m_j$, neglecting the pitch angle averaging, see Eq. (A2). Astrophysical photon spectra typically exhibit features, such as a spectral break (such as for GRBs) or a maximum (such as for the CMB) at a certain $\hat{\varepsilon}$, whereas the cosmic-ray primaries typically follow a power law. As a consequence, given a cross section $\sigma(\epsilon_r)$ at a certain energy $\epsilon_r$, primaries with the energy $E_j \simeq \epsilon_r m_j/\hat{\varepsilon}$ will be selected to interact, and the secondary spectra will exhibit spectral excesses corresponding to that primary energy. In that sense, $\sigma(\epsilon_r)$ as a function of the PRF is the required input for astrophysical applications, and a definition of a target photon spectrum in the nucleus' rest frame does not make sense. Larger values of $\epsilon_r$ just mean that the spectral features will appear at higher energies in $E_j$ if the cross section is significantly large there. For all practical cases, one therefore needs the cross section in the region around the GDR up to the point where it significantly drops. This can be seen *e.g.* in Fig. 6 by comparing the PEANUT cross section curve with the measurement for $^{23}$Na, which are practically identical up to the maximally measured energy. The difference in the disintegration length is nevertheless large, as the contribution beyond $\epsilon_r \simeq 30$ MeV, which is missing in the measurement case, cannot be neglected (and will be re-distributed by the pitch angle averaging). The direct correlation $E_j \propto \epsilon_r$, translating cross section peaks into the disintegration rate, can be best seen in the CMB cases in Fig. 6.

### Appendix B: Situation on Experimental data and model calculations

Here we summarize the status on experimental data and theoretical models.

#### 1. Experimental data

EXFOR [20] is a nuclear reaction database, aimed to be a complete collection of experiments and theoretical evaluations performed during the last half century. The effort to maintain and standardize the data collection is a world-wide collaborative effort between various nuclear centers. In this work, we assume that this database is to a large extent complete and our result is not distorted by one or few missing entries.

The database contains experimental data points, model-evaluated data, ratios of cross sections and other data categories. For our purpose we apply the following criteria to the data selection:

- only real experimental data, no evaluated cross sections;
- no reaction combinations, ratios or partial measurements;
- full unfolded cross sections in barns;
- energy range of the measurement has to cover the GDR peak.

Further, we create two selections (EXFOR, $\sigma_{\rm abs}$) and (EXFOR, any), where the first includes only measured absorption cross sections $\sigma_{\rm abs}$ and the latter requires at least one inclusive cross section to be measured. With these criteria, EXFOR contains 14 absolute cross sections and 47 of the second category up to masses of $^{56}$Fe. (EXFOR, any) can be used to estimate the number of more certain absorption cross sections from nuclear reaction models.

#### 2. Theoretical models

Monte Carlo particle transport codes, such as FLUKA [26, 27], MCNP [29] or PHITS [30] use evaluated nuclear data files to compute interaction rates and ICPE for exclusive reaction cross/sections. FLUKA contains a comprehensive photo-nuclear cross section library based direct on data, photo-neutron evaluation and parameterizations for a large set of isotopes [23, 24]. It is coupled to the ICPE code PEANUT to generate final state distributions. Comparisons of PEANUT cross sections reveal a very good agreement to available data on $\sigma_{\rm abs}$. MCNP employs in a similar manner ENDF-B-VII.1 [21] as evaluated nuclear data library, based on reaction model calculations using the GNASH code system. For photo-nuclear data file for PHITS is JENDL/PD-2004 [22], which has often good agreement with data but also shows some interpolation or fitting artifacts for light and intermediate nuclei.

Our current baseline model is based on cross sections extracted from TALYS 1.8 for nuclei with $A \geq 12$ and CRPropa2 lighter nuclei. TALYS 1.8 was configured to use the Kopecki-Uhl generalized Lorentzian description, as it is recommended in [14] in order to better predict cross sections non only in the GDR region. Photo-nuclear cross sections for light nuclei in CRPropa 2 are compiled from various references, as reported in [19], for a total of 19 primary isotopes and 69 inclusive cross sections. The TALYS 1.6 cross sections are currently used in CRPropa 3, to predict photodisintegration products of all available exclusive channels: proton, neutron, deuterium, tritium, helium-3 and helium-4 and combinations thereof; the parameters used to model the giant dipole resonance have been adjusted to match the cross sections reported in [14], as explained in [8]. The *SimProp* code uses an approximation scheme to implement TALYS cross sections, as reported in [6].

The PSB model [5], which is tailored for cosmic-ray propagation problems, represents each isobar with the most abundant stable isotope, starting from $^{56}$Fe down to $^{2}$H, excluding the unstable masses $5 \leq A \leq 8$. This model approximates the cross sections for one- and two-nucleon emission with a Gaussian shape in the low energy range ($2 \leq \epsilon_r \leq 30$ MeV), while the cross sections for multi-nucleon emission in the high energy range ($30 \leq \epsilon_r \leq 150$ MeV) are constant. In *SimProp* the list of isobars matches [5], but the corresponding elements are assigned from Table 1 in [31] by choosing the isotope that corresponds to the lowest energy threshold for the emission of one proton. For the purpose of the present work, we have slightly changed the criterion for choosing the element with respect to what has been done in *SimProp* or in the original PSB model, that allowed for example for $A \to A' = A-1$ with an increasing number of protons with respect to the parent nucleus, by choosing descending elements in the chain corresponding to the mass in the original list.

### Appendix C: Nuclear disintegration in a GRB

Our GRB model follows Refs. [28, 32], extended by the explicit simulation of the nuclear cascade. Here we only sketch the key ingredients, whereas details of the computation method and the efficient treatment of the particle interactions will be presented elsewhere [33].

We solve a system of partial differential equations, which, for particle species $i$ (in our case nuclei), reads

$$\frac{\partial N_i}{\partial t} = \frac{\partial}{\partial E}\left(-b(E)N_i(E)\right) - \frac{N_i(E)}{t_{\rm esc}} + \tilde{Q}_{ji}(E)\,, \quad \text{(C1)}$$

where $b(E) = Et_{\rm loss}^{-1}$ with the energy loss rate $t_{\rm loss}^{-1} = E^{-1}|dE/dt|$ and $t_{\rm esc}^{-1}$ the escape rate. The equation is

solved for the differential particle densities $N_i$ as a function of time, evolved until the steady state is reached. The coupled system arises because the injection term

$$\tilde{Q}_{ji}(E) = Q_i(E) + Q_{ji}(E) \tag{C2}$$

allows for injection from an acceleration zone $Q_i$, as well as for injection from other species $j$ with the term $Q_{ji}$, such as from photodisintegration. In this work, we only inject $^{56}$Fe into the system with a power law $E^{-2}\exp\left(-(E/E_{\rm Fe,max})^2\right)$, where $E_{\rm Fe,max}$ is determined by balancing the dominant energy loss process with the acceleration rate $t_{\rm acc}^{-1} = \eta c/R_L$. Here $R_L$ is the Larmor radius and a relatively high $\eta \simeq 10$ has been chosen to reproduce the composition transition observed by Auger [3].[1] The target photons are assumed to follow a broken power law with a break at 1 keV in the shock rest frame between the power law index $-1$ (low energy) and $-2$ (high energy). Note that we choose the minimal photon energy low enough such that photodisintegration will always dominate at the highest energies. The baryonic loading is assumed to be ten, which means that there is ten times more energy injected into iron compared to electrons, and energy equipartition between magnetic field, electron and photon energy is assumed.

For the nuclear energy losses, we include synchrotron losses, adiabatic losses, pair production losses, and photonuclear losses, where we distinguish between photodisintegration (focus of this work, dominated by the GDR) and photo-meson production (dominated by the $\Delta$-resonance and other processes) by $\epsilon_r$. The photodisintegration is implemented in different models, as discussed in the main text of this work. We include photo-meson production based on SOPHIA [34] using an improved and extended version of Ref. [35] with a superposition interaction model assuming that the cross section scales $\propto A$. While such an approach is state-of-the-art in the literature, see *e.g.* Refs. [13, 19], it is clear that it needs improvement from the interaction model perspective. Note that photo-meson production leads to the disintegration of nuclei as well, where the characteristics (secondary nuclei multiplicities and distributions) can be different; however, for the chosen parameters, the photodisintegration dominates. We furthermore include beta decays of radioactive isotopes and spontaneous emission channels which are relevant on the dynamical timescale [36].

In order to discuss the ejected cosmic-ray composition, we assume that cosmic rays can either escape as neutrons (which are not magnetically confined) or, directly from the borders of the production region within their interaction length or Larmor radius (whatever is smaller) [28], which leads to relatively hard spectra acting as a high-pass filter [12]. This is, in a way, the most conservative assumption one can make, as, for instance, diffusion would enhance the escape at lower energies, or the magnetic fields may decay quickly enough that all particles can escape. More detailed discussions of the astrophysical implications including the neutrino production will be presented elsewhere [37].

For an efficient computation, we need to pre-select the isotopes which are dominantly populated. Our isotope selection scheme is a fully automated recursive algorithm starting (in this case) with $^{56}$Fe, following all disintegration and beta decay paths recursively. We also allow for mixed paths, meaning, for instance, that a disintegration may be followed by beta decay and then disintegration again. Since one isotope has typically very many (disintegration) branchings into daughters, some of these being very small, we impose a cutoff on the secondary multiplicity (number of secondaries produced on average) at a value of 0.01. As a further complication, the multiplicities, *i.e.*, the distribution of secondaries, depend on $\epsilon_r$. In order to be as inclusive as possible, we therefore repeat the procedure for several values of $\epsilon_r$ in the relevant interaction energy range.[2] We also tested other methods (such as based on the fractional contribution or picking the leading channels) with similar results. However, the result will depend on the choice of the control parameter, which is the threshold multiplicity here. As it turns out that intermediate mass number isotopes have a large number of daughter nuclei with relatively small multiplicities off the main diagonal, one cannot pick a too large threshold value as it would stop the cascade. Fast spontaneous emitters (faster than any other process at any given energy) are automatically integrated out by recursively following their decay paths to the next isotope which is explicitly treated. For example, for the TALYS disintegration model, the software uses 481 isotopes, about 41000 inclusive disintegration channels and about 3000 photo-meson channels as primary input, selects 233 isotopes, and attaches 4943 disintegration, 10 beta decay (relevant on the GRB timescale) and 1344 photo-meson channels to them. With this level of complexity and the explicit treatment of the nuclear cascade, it is clear that our technology is currently more advanced that any other method in the literature for the simulation of the sources of the UHECR nuclei themselves.

The choice of isotopes in Fig. 1 labeled "Astro, priority 1" and "Astro, priority 2" has been obtained with a similar method by repeating the above recursive procedure for a number of possible injection elements: we inject for each atomic number the most abundant stable isotope. The multiplicity threshold has been chosen to be 0.2 for priority 1 and 0.05 for priority 2. As these numbers are larger than the threshold above, this list of isotopes is smaller than the one actually used for the GRB compu-

[1] Choosing a milder cutoff in the injection spectrum reduces the required $\eta$.

[2] Actually we integrate over the pitch angle between nucleon and photon and use the pitch angle averaged multiplicities; the pitch angle enters the relationship between the photon/nucleus' energies and $\epsilon_r$, see Eq. (A2).

tation. However, one can easily see by comparing the blue isotopes in Fig. 1 with the ones in Fig. 3, upper right panel, that these are actually the most populated ones in a realistic simulation. Note that the main difference between these plots is that the extension of the nuclear cascade to low mass numbers depends on the energy in the GRB, and that only iron has been injected in the GRB case. We expect that our isotope priority selection is robust in the sense that taking into account different $\epsilon_r$ and being inclusive in the selected isotopes, they hardly depend on the shape of the target photon spectrum.

We also show two models used in Fig. 4 in Fig. 5: the "systematic offset" and "random systematics" (one example) cases. The uncertainties in the cross sections are inspired by Fig. 2, which are of the the order of a factor two. For the random offsets panel, we vary all unmeasured absorption cross sections randomly between 0 and 2 of their nominal values, and all absorption cross sections with only some partial information (inclusive channels) between 0.5 and 1.5. Note that we re-scale all absorption and inclusive cross sections for one isotope with the same number, as we obtain otherwise inconsistencies between the escape and re-injection rates. We can read off from the figure that certain isotopes will be more highlighted then others, while the total cascade looks similar to the nominal TALYS model. For the "systematic offset" panel, we systematically choose the minimal value in these cases, which leads to a systematic suppression of the nuclear cascade. Here the nuclear cascade will stop because of the cross section suppression, and intermediate and light elements will not be populated.

### Appendix D: Disintegration rates for alternative elements

To illustrate a second example in addition to Fig. 2, we compare cross sections of $^{23}$Na and $^{23}$Mg in Fig. 6. Contrary to the double-magic $^{40}$Ca, $^{23}$Na is not expected to be spherical, where GDR cross sections can be sufficiently approximated using a single peak. Therefore, the models with only one main Lorentzian or Gaussian peak do not reproduce the measurement, as it is the case for the PSB model. Without dedicated Lorentzian fits, TALYS doesn't reproduce the shape of the GDR peak, adding an additional, unphysical, peak at $\sim$ 14 MeV. The latter can be attributed to the strength parameter setting and can be potentially corrected through individual tuning. However, such modification would alter the model for a single isotope without improving the predictive power for other isobars. The PEANUT prediction reproduces very well the available measurement [38] on $^{23}$Na, while the box model is insufficient and yields factor of two smaller disintegration rates. For the unknown $^{23}$Mg cross section, TALYS, PSB and the box model predict identical cross sections, while PEANUT falls back to a parametrized form, producing a significantly different result. Updated versions of PEANUT and FLUKA[3] estimate unknown cross sections with the Isobaric Analog State (IAS) approach, where nuclei with identical wave functions, and therefore, with a similar isospin and level structure are treated analogously. If such an equivalence case is detected, the model maps unknown cross sections of nuclei to a known IAS nucleus. The effect of IAS is illustrated in the right panel Fig. 6 and results in up to a factor three higher disintegration rates in the case of PEANUT. If IAS is a valid concept for photon projectiles, several additional cross sections can become known to higher precision without the need for individual measurements.

[3] Private communication with Alfredo Ferrari (07/2016)

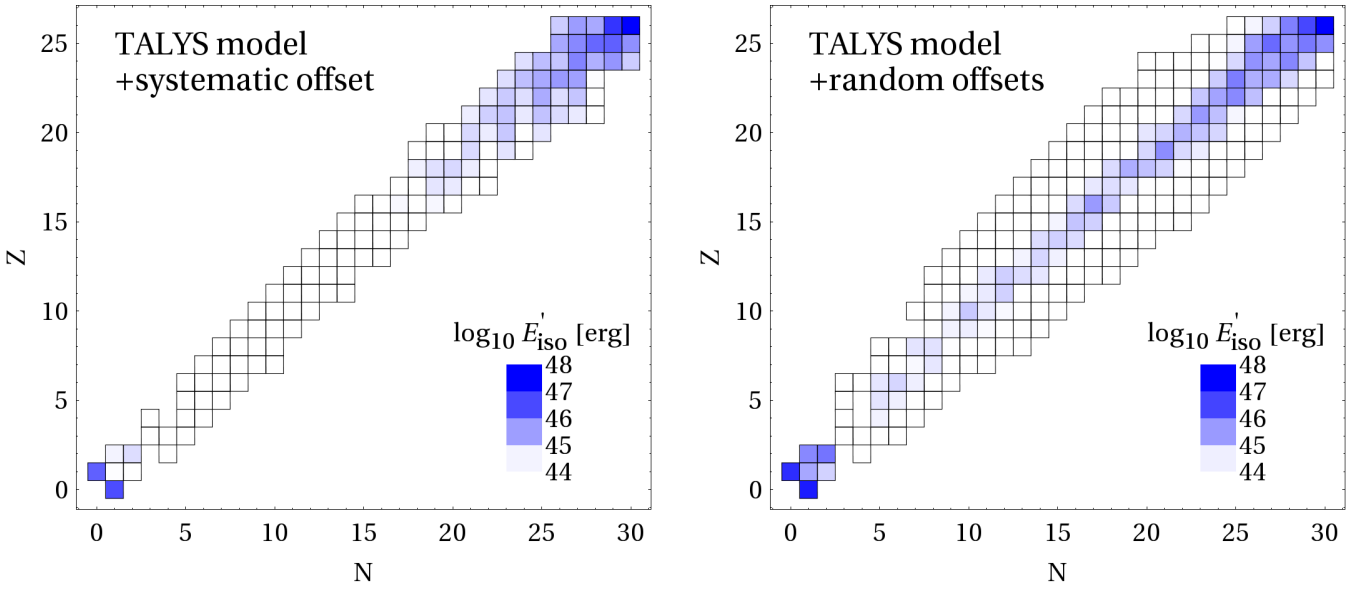


FIG. 5: Same as Fig. 3 for different model assumptions, see main text.

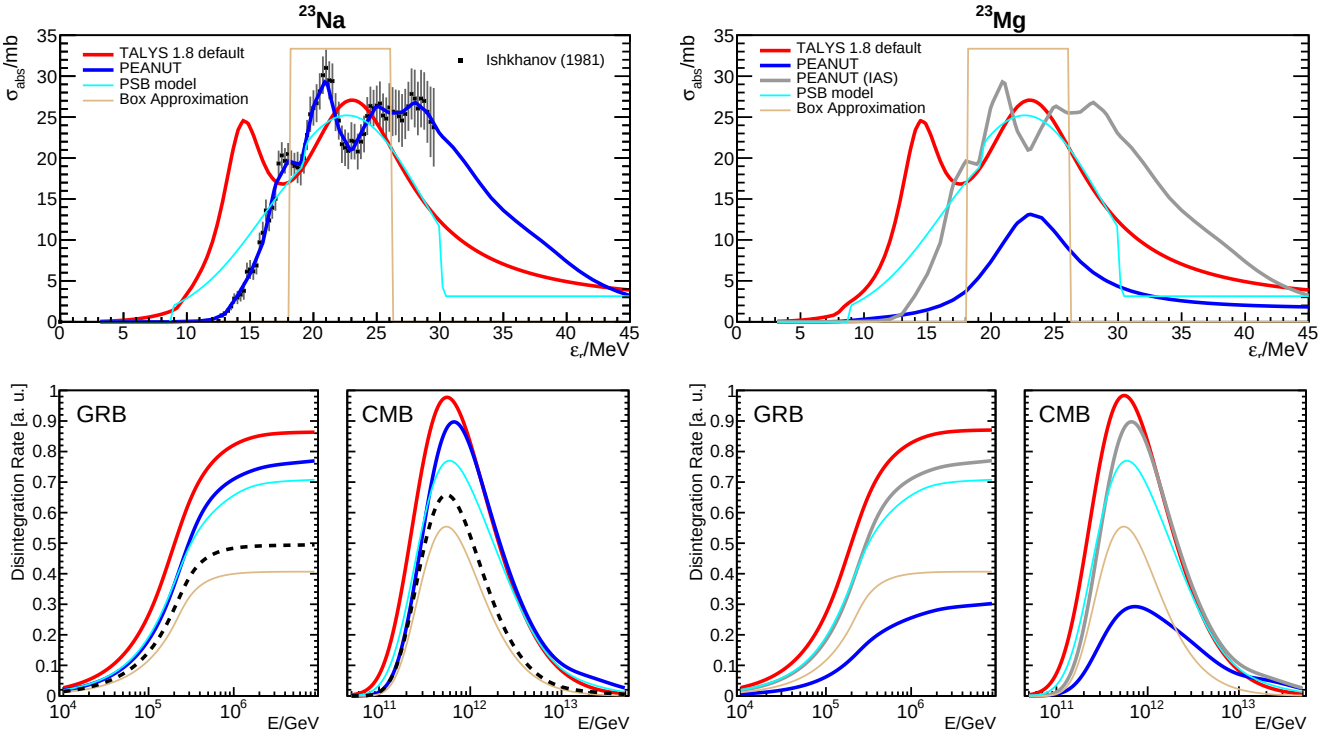


FIG. 6: Same as in Fig. 2, for $A = 23$.